CHEMISTRY OF MATERIALS

pubs.acs.org/cm

Article

Mechanism of the Temperature-Dependent Self-Assembly and Polymorphism of Chitin

Aarion Romany, Gregory F. Payne, and Jana Shen*

Cite This: *Chem. Mater.* 2023, 35, 6472−6481

Read Online

ACCESS | Metrics & More | Article Recommendations | Supporting Information

ABSTRACT: Chitin is the second most abundant natural biopolymer. Its crystalline structures have been extensively studied. However, the mechanism of chitin's self-assembly is unknown. Here, we applied all-atom molecular dynamics to study chitin's self-assembly process at different temperatures. Strikingly, at 278 K, an amorphous aggregate was formed, whereas at 300 K single-sheet and at 323 K both single-sheet and multisheet nanofibril regions were formed. The nanofibrils contain antiparallel, parallel, or mixed orientation chains, with antiparallel being slightly preferred, recapitulating chitin's polymorphism observed in nature. The inverse temperature dependence is consistent with a recent experiment conducted in the aqueous KOH/urea solution. The analysis suggested that the multisheet nanofibrils are assembled by stacking the single nanofibril sheets, which are formed through two types of pathways in which hydrophobic collapse either precedes or is concomitant with the increasing number of interchain hydrogen bonds and solvent expulsion. Furthermore, the antiparallel and parallel chains are mediated by different interchain hydrogen bonds. The analysis also suggested that the inverse temperature dependence may be attributed to the hydrophobic effect reminiscent of the low critical solution temperature phase behavior. The present study provides a rich, atomic-level view of chitin's polymorphic self-assembly process, paving the way for the rational design of chitin-derived novel materials.

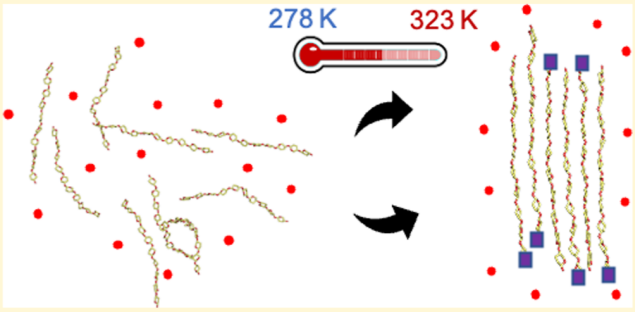

INTRODUCTION

Following cellulose, chitin is the second most abundant naturally occurring polymer on earth. Owing to the biodegradability and high tensile strength, chitin derivatives have been found in diverse applications, such as tissue engineering, drug carriers, cosmetics, wound dressing, and recently pickering emulsion.[1−6] However, to make functional materials from chitin, a challenge is to find effective and environmentally friendly ways to dissolve it in solution,[7,8] and once dissolved, another challenge is to achieve controlled fabrication.[4,9] Thus, a detailed understanding of chitin's self-assembly mechanism is important.

Chitin is a homopolymer composed of β-(1−4)-linked *N*-acetylglucosamine units. Native chitin is a semicrystalline fibril material consisting of crystalline (microfibers) and amorphous regions, where the crystal is composed of a 2−5 nm thick fibril made up of 18−25 chains.[4] Chitin's crystalline structures have been studied by numerous groups using electron microscopy and X-ray diffraction for over 50 years, which revealed three (α, β, and γ) polymorphic forms depending on the natural sources (Figure 1a,b).[10−18] The most abundant allomorph is α-chitin, which contains antiparallel chains in the crystalline structure and can be found in hard shells of various crustaceans and cell walls of select fungi[19] (Figure 1a). The second common allomorph is β-chitin, which contains parallel chains and can be often found in soft protein-rich structures such as squid pens and tube worms[20] (Figure 1a). γ-Chitin is the rare allomorph, which contains both parallel and antiparallel chains and has been found in the cocoon fibers of beetle and stomach of squid[13,18] (Figure 1a). α-Chitin is less susceptible to intracrystalline swelling and is always obtained in recrystallization from solution, which has been attributed to the presence of intersheet hydrogen bonds (h-bonds).[13,19] Interestingly, although having both chain orientations, γ-chitin is more similar to α than β-chitin in the X-ray diffraction pattern and thermal stability.[13] More recent studies using solid-state NMR spectroscopy suggest that chitin in the natural environment may be more polymorphic than previously thought based on the X-ray diffraction data.[21,22] The NMR shift analysis of 45 chitin subforms in fungal cell walls demonstrated significant structural heterogeneity and deviations from that electron microscopy data.[22]

Two recent studies of Cai and co-workers[23,24] based on a variety of experimental techniques including atomic force

Received: May 29, 2023
Revised: July 18, 2023
Published: August 1, 2023

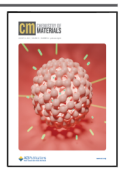

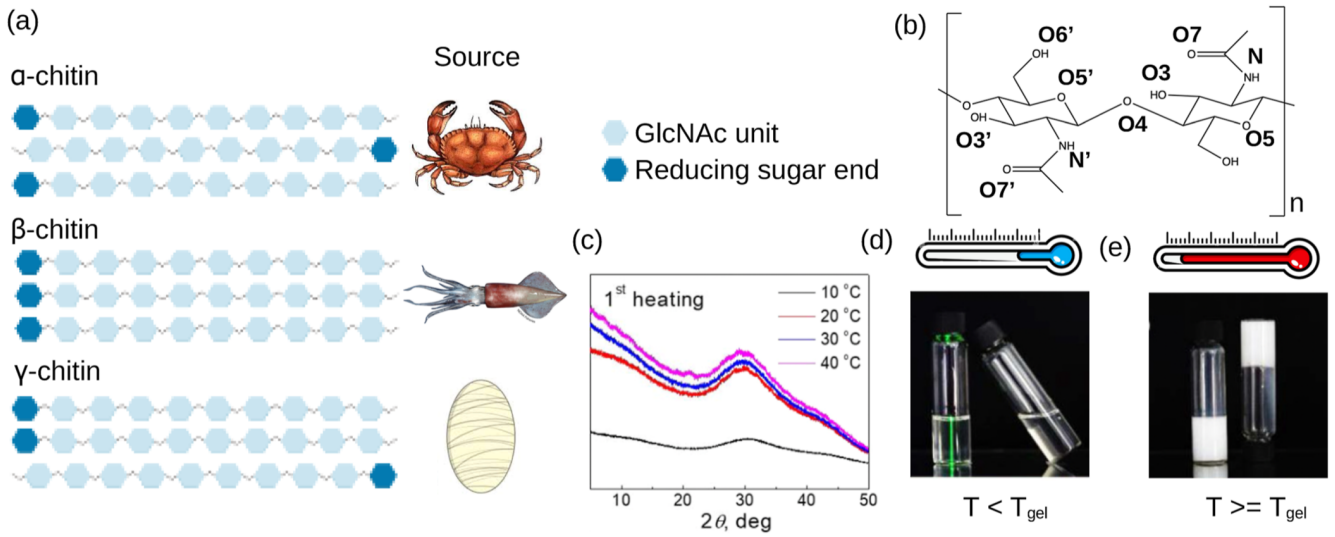

Figure 1. Schematics of chitin's polymorphism and heat-induced gelation. (a) Three allomorphs of chitin and their common natural sources.[10−18] The chain direction is illustrated by the reducing sugar end (blue). (b) Chemical structure of β(1,4)-linked acetylglucosamine (GlcNAc) dimer, the building block of chitin. (c) Powder X-ray diffraction pattern of chitin solution (10 °C, dissolved in aqueous KOH/urea) and heat-induced gels in the first heating process. (d) Below the gelation temperature (T_{gel}), chitin solution remains transparent. (e) Above T_{gel}, chitin solution turned to a white solid gel. Images in (c,d,e) are taken from ref 23. Reprinted or adapted with permission under a Creative Commons CC-BY 4.0 from ref 23 Copyright 2020 Elsevier.

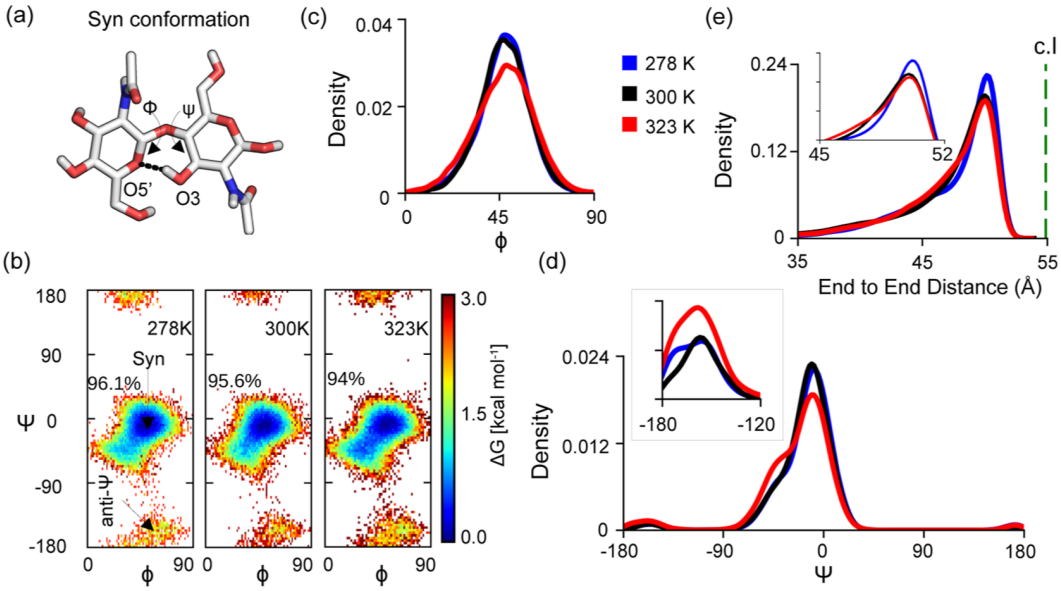

Figure 2. Stiffness of the dissolved 10-mer chitin chains in water is slightly reduced at 323 K. (a) Structure of an acetylglucosamine dimer in a *syn* conformation. The glycosidic backbone Φ and Ψ angles as well as the O3H−O5′ intramolecular h-bond are indicated. In the alternative anti-Ψ conformation, the sugar rings are perpendicular to each other.[29] (b) FES as a function of the Φ and Ψ angles for the chitin chains in water at three temperatures. The *syn* and anti-Ψ regions are indicated. The average percent population of the *syn* conformation calculated from bootstrap analysis of the three simulation runs at each temperature is given. Following ref 29., the *syn* conformation was defined using the range of [−90, 125°] for the Φ and [−100, 90°] for the Ψ angle. Probability distributions of the (c) Φ (top) and (d) Ψ (bottom) angles of the dissolved chitin chains at 278 (blue), 300 (black), and 323 K (red). (e) Probability distributions of the end-to-end distances (between the O1 atom of the first and the O4 atom of the last acetylglucosamine unit in the chitin chain) of the dissolved chains at 278, 300, and 323 K. Data for each temperature is the aggregate of the initial 50 ns of the three simulation runs. Any chains that are within 4.5 Å of another were excluded. This was further confirmed by visual inspection. The theoretical contour length is indicated as a green dashed line.

microscopy, fluorescence microscopy, and wide-angle X-ray diffraction examined the gelation behavior of α- and β-chitin at different concentrations, temperatures, and aging times. Surprisingly, they found that gelation of α-chitin dissolved in the aqueous KOH/urea solution is heat-induced—the diffraction curve of the chitin solution is smooth with minimum intensity at 283 K (10 °C) but the intensity increases dramatically with temperature between 293 K (20 °C) and 313 K (40 °C)[23] (Figure 1c,d). A similar behavior was observed for β-chitin dissolved in the KOH/urea solution, although the self-assembled hydrogels were made up of α-chitin nanofibrils.[24] These observations seem to contradict the

https://doi.org/10.1021/acs.chemmater.3c01313
Chem. Mater. 2023, 35, 6472−6481

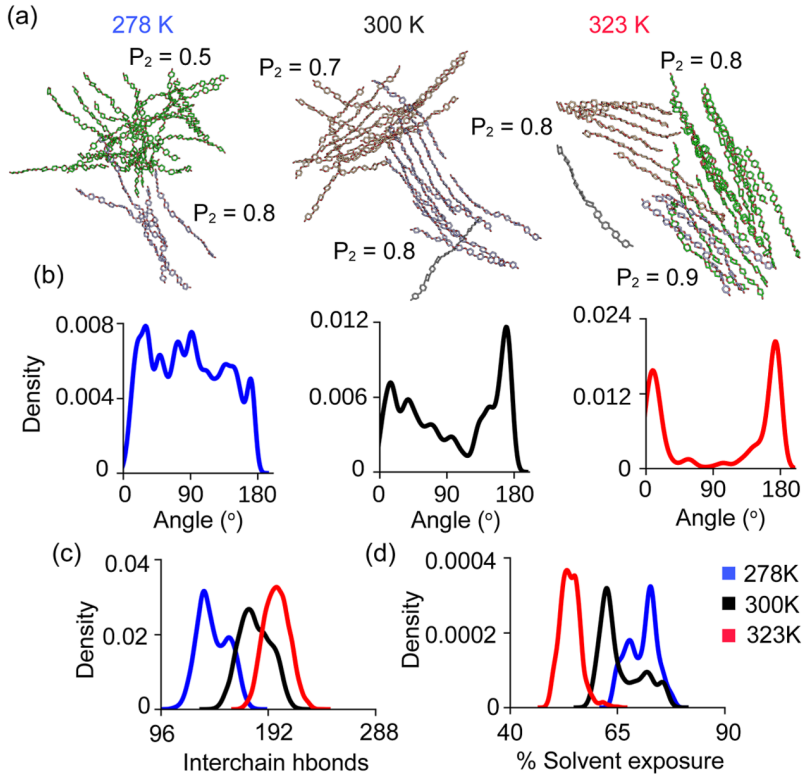

Figure 3. Temperature effect on the self-assembled structure, hydrogen bonding, and solvent exclusion between chitin chains. (a) Representative final snapshots from the simulations at three temperatures showing the formed aggregate and nanofibril regions. Only the sugar rings and glycosidic linkages are shown for clarity. Snapshots at 278, 300, and 323 K are taken from run 3, 3, and 2, respectively. Ordered regions (shown in different colors) are identified in the aggregates, with the local P_2 order parameter given. $P_2 > 0.7$ indicates a mostly ordered state. The final 100 ns of simulation time was used for the P_2 calculation. (b) Probability distribution of the angle between chains at three temperatures. (c) Probability distribution of the total number of interchain h-bonds for the 24 chitin chains at three temperatures. (d) Probability distribution of the percentage solvent exposure of the 24 chitin chains at three temperatures. Solvent exposure was calculated as the SASA of the chitin heavy atoms relative to the value calculated following the energy minimization of the system. For (b,c,d), the final 100 ns of three trajectories was combined for each temperature.

common belief that hydrogen bonding, which is thought to be the driving force for the association of chitin chains,[19] weakens with increasing temperature. To provide an explanation, the authors hypothesized that the heat-induced gelation is due to increased hydrophobic association of chitin chains at increasing temperature.[23,24]

Compared to a large body of experimental work on chitin's physicochemical properties, theoretical investigations have been sparse. A few studies based on molecular dynamics (MD) simulations starting from a prebuilt model crystallite structure of α-chitin examined the decrystallization thermodynamics,[25] hydrogen-bonding pattern in the nanofiber,[26] or binding of a short chitosan oligomer.[27] Based on the prebuilt α- and β-nanofibers, a recent reactive MD study investigated the different mechanical properties of the two crystalline forms.[28] Distinct from the published computational work, we performed MD simulations of chitin self-assembly from water at different temperatures to understand chitin's polymorphism and heat-induced self-assembly. Strikingly, our simulations captured the formation of nanofibril in α, β, and γ allomorphs, and consistent with the experiments of Cai and co-worker,[23,24] the self-assembly did not occur at 278 K (5 °C), while the nanofibril formation is more ordered at 323 K (50 °C) as compared to 300 K (27 °C). The analysis revealed the temperature-dependent conformational dynamics and self-assembly process of the chitin chains. Furthermore, the relative orientations of the chitin chains in the nanofibers were found to be attributed to the distinct interchain hydrogen bonds (h-bonds). Together, our data provides a rich and intimate view of the temperature-dependent polymorphic self-assembly process of chitin.

RESULTS AND DISCUSSION

Stiffness of the Dissolved Chitin Chains in Water is Slightly Enhanced at 323 K. The self-assembly simulations of chitin were initiated from 24 chains, each comprised 10 *N*-acetyl-glucosamine units randomly distributed in a 85 Å × 85 Å × 85 Å cubic box filled with water and periodically replicated in three dimensions. The simulation was performed at three temperatures, 278, 300, and 323 K, and for each temperature, three independent simulations were initiated from different random velocity seeds. Each simulation was continued until the total solvent accessible surface and the total number of interchain hydrogen bonds plateaued (i.e., converged), for 3 μs at 278 K and 2 μs at 300 and 323 K (Figures S1 and S2). Since the simulations were conducted prior to the comparison with experiments by Cai and co-workers,[23,24] the temperatures used are somewhat different (283, 293, and 313 K in experiments). This, however, should not affect the comparison of the temperature-dependent trend. Another difference between our simulations and Cai's experiments is that while water is the

https://doi.org/10.1021/acs.chemmater.3c01313
Chem. Mater. 2023, 35, 6472−6481

only solvent in our simulations, aqueous solution with 20 wt % KOH/4 wt % urea was used in the experiments.[23,24]

We first investigated if the conformation and/or dynamics of the dissolved chitin chains is affected by temperature. To do so, we calculated the Φ and Ψ dihedral angles around the backbone glycosidic bond (Figure 2a) of the chitin chains before the self-assembly process began (the initial 50 ns data was used). Following the convention used in the previous work,[29,30] Φ and Ψ torsion angles are defined as H1′-C1′-O4-C4 and H4−C4−O4−C1′, respectively (Figure 2a). The free energy surface (FES) as a function of Φ and Ψ (Figure 2b) displays a global minimum near (45, 0°) for all three temperatures, suggesting that the dominant conformation the chitin chains assume is *syn*, which is in agreement with the recent NMR and simulation data for $\beta(1 \rightarrow 4)$-linked disaccharides in aqueous solution[30] as well as our previous simulations of chitosan chains in solution.[29]

A closer examination of the FES reveals that the probability of the anti-Ψ region is slightly higher at 323 K (Figure 2b). This is related to the slightly broader distribution of the Φ angle and greater sampling of the alternate Ψ angles at 323 K as compared to 278 and 300 K (Figure 2c). The average *syn*-state population from the bootstrap analysis of the three simulation runs is 96.1% at 278 K, 95.6% at 300 K, and 94% at 323 K (Figure 2b), compared to about 96% *syn* population for the neutral fully deacetylated 10-mer chitosan chains.[29] These data suggest that the solution chitin chains are similarly stiff as the neutral chitosan chains; however, the stiffness is slightly decreased at 323 K.

To investigate if the temperature also affects the dimension of the solution chitin chains, we calculated the distribution of the end-to-end distance (Figure 2d). The peak of the distribution for 323 K is slightly left-shifted and lower compared to 278 and 300 K, demonstrating that the chains are slightly less extended and more flexible at 323 K, which corroborates with the more flexible backbone discussed earlier (Figure 2b,c).

Increasing Temperature Promotes Chitin's Nanofibril Formation in Water. We next examined the self-assembly process of the chitin chains at three temperatures. At the end of all simulation runs, the chitin chains formed a single aggregate with at most one chain left in solution (see representative final snapshots in Figure 3a). To examine the degree of order, we first calculated the distributions of the angles between any two chitin chains. At 278 K, the distribution is nearly uniform with many local peaks between 0 and 180°, indicating that the chains are largely randomly oriented (Figure 3b). In contrast, the distribution at 300 K is bimodal, showing the major mode (sharp peak) near 180° and the minor mode (lower and broader peak) near 0°, which indicates that many chains are antiparallel and some are parallel to each other (Figure 3b). At 323 K, the bimodal distribution is more sharply peaked; the minor peak near 0° has an increased height and decreased width, indicating that the chains are mostly aligned antiparallel/parallel to each other with the antiparallel orientation being slightly favored as the 300 K distribution (Figure 3b). This is consistent with the experimental observation that α-chitin which contains all antiparallel chains is the most common and stable allomorph.[13,19]

To quantify the degree of order, we calculated a P_2 order parameter analogous to the global order parameter used for characterizing nematic liquid crystals and amyloid nanofibrillation[31] (see Methods and Protocols). P_2 is bound between 0 and 1, where 0 indicates a completely disordered state with the chains randomly oriented relative to each other and 1 indicates a perfect fibrillar state in which the chains are parallel or antiparallel to each other. Following our previous work on amyloid fibrillation,[31] we consider the chitin chains as in a fibrillar or an amorphous state if P_2 is > 0.7 or <0.3, respectively. The P_2 values for the aggregates formed in the three runs at 278, 300, and 323 K are 0.4/0.4/0.5, 0.3/0.2/0.6, and 0.8/0.8/0.4, respectively (Table S1).

Visualization of the aggregates suggested that the chitin chains can be grouped into two or more regions, and some of the regions are remarkably ordered, resembling nanofibrils (Figure 3a). Thus, we calculated the order parameter for each region (Table S1). At 278 K, two regions, one comprised 4 or 5 chains and another one comprised 19 or 20 chains, were identified in the three runs. While the first region is somewhat ordered (P_2 of 0.7 or 0.8 in two runs), the second region is closed to being amorphous (P_2 of 0.4 or 0.5) in all three runs (Figure 3a and Table S1). At 300 K, 2−5 regions were identified in the three runs and most of them were more ordered than those formed at 278 K (Figure 3a and Table S1). Run 1 resulted in three highly ordered regions comprised 3 or 7 chains (P_2 of 0.9 or 1.0), one somewhat ordered region (P_2 of 0.7), and one amorphous region. Run 2 resulted in one highly ordered region of 5 chains (P_2 of 0.9) and the remaining ones are amorphous. Run 3 resulted in two ordered regions comprised 10 and 13 chains (P_2 of 0.7 and 0.8). At 323 K, all three runs showed highly ordered regions with P_2 of 0.8 or greater. The largest region contains 21 chains with a P_2 value of 0.8, followed by the regions with 14 and 10 chains and respective P_2 values of 0.8 and 0.9 (Figure 3a and Table S1). Comparing the data across the three temperature, it is evident that larger, more ordered (i.e., fibril-like) regions are formed with increasing temperature. In the discussion that follows, we will refer to the regions with P_2 > 0.7 as nanofibrils except for those from the 278 K simulations which lack of specific interchain h-bonds (see later discussion).

Interchain Hydrogen Bond Formation Increases and Solvent Accessibility Decreases with Increasing Temperature. To examine the effect of temperature on chitin's self-assembly, we also calculated the probability distributions of the total number of interchain h-bonds and the percentage solvent exposure of the 24 chitin chains based on the last 100 ns of the simulations at three temperatures. The peak of the distribution of the interchain h-bond number is shifted toward larger values as temperature increases from 278 to 323 K (Figure 3c), indicating that more interchain h-bonds are formed with higher temperature, which is consistent with the increased order of the formed aggregate (Figure 3a). Although this relationship between temperature and hydrogen bonding may seem contrary to the common belief, it is in agreement with the experimental observation that the sol−gel transition of dissolved chitin occurs above, rather than below, a gelation temperature (around 288 K for dissolved α-chitin).[23,24]

Next, we examined the percentage solvent exposure of the 24 chitin chains, which is calculated as their solvent accessible surface area (SASA) relative to the fully solvent exposed state. As temperature increases, the distribution is shifted toward smaller values (Figure 3d), indicating that the chitin chains become more buried or in other words, more water is displaced from the first solvation shells. This suggests that the temperature-dependent self-assembly of chitin may be

https://doi.org/10.1021/acs.chemmater.3c01313
Chem. Mater. 2023, 35, 6472−6481

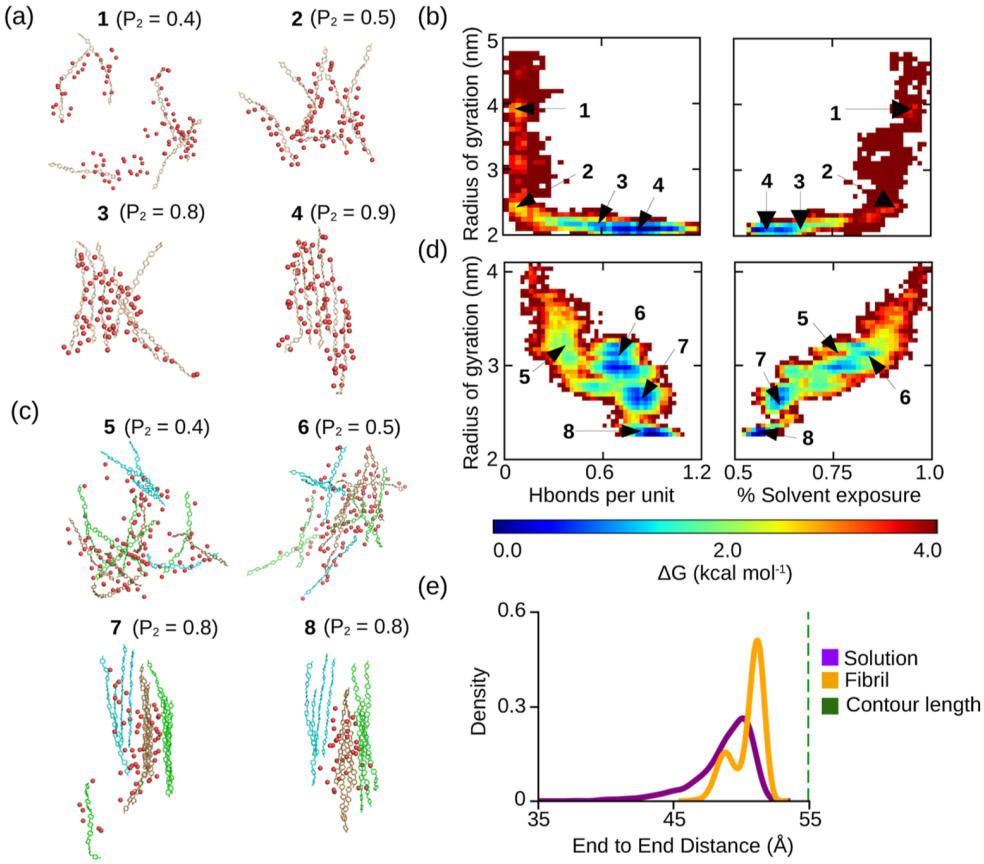

Figure 4. Self-assembly pathway of a single-sheet nanofibril of chitin follows two mechanisms. (a,c) Representative snapshots extracted from the local minimum regions in the FES to illustrate the formation of 6-chain (a, snapshot 1−4) and 10-chain (c, snapshot 5−8) single-sheet nanofibrils. Red spheres represent water molecules in the first hydration shell defined within a 3.4 Å radius from any heavy atom of the chain. (b,d) FES spanned by the radius of gyration and the number of h-bonds per GlcNAc unit (left panel) or the percentage solvent exposure (right panel) of the chitin chains. The number of h-bonds per unit was calculated by dividing the total number of interchain h-bonds by the number of chains and the degree of polymerization per chain (the two end units were ignored). The percentage of solvent exposure was calculated using SASA (see Figure 3). (e) The distribution of the end-to-end distance of the chitin chain in solution (purple) and fibril (brown) state. The green dashed line represents the theoretical contour length of 55 Å for a 10-mer chitin chain. Data for (a,b,e) and (c,d) refer to the chains in the nanofibril region 1 formed in the 323 K simulation run 2 and 3, respectively.

explained by the hydrophobic effect. In the classical view, the association of small hydrocarbons in water is driven by the hydrophobic effect (i.e., $-T\Delta S$) which becomes more negative with increased temperature up to a certain temperature.[32,33] In a recent MD study; however, Durell and Ben-Naim found that between 280 and 360 K, the free energy of bringing together hydrophilic solutes that are directly h-bonded to each other also becomes more negative with increasing temperature as does for two hydrophobic solutes.[34] Their analysis[34] demonstrated that the increase in the entropic term $T\Delta S$ is due to the release of h-bonded water as the solutes form h-bonds among themselves, which may explain the increased interchain h-bonds and displacement of the first-solvation-shell (i.e., bound) water for the temperature-dependent self-assembly of chitin. Given the high correlation between interchain h-bonding and solvent accessibility, we begin to see the important role solvent plays in the self-assembly of chitin.

Formation of Single-Sheet Nanofibrils Proceeds Via Two Distinct Mechanisms. In theoretical studies of protein folding pathways, one often considers a low-dimensional FES spanned by order parameters such as the fraction of native contacts (ρ) and the radius of gyration (R_g). Based on the shape of the FES spanned by ρ and R_g, two types of mechanisms have been proposed for protein folding.[35] In the first mechanism which is represented by a L-shaped FES,[35] protein collapses in solvent first before rearrangement to increase the native contacts. In the second mechanism which is represented by a diagonally shaped FES,[35] the hydrophobic collapse and native contact formation are concomitant. It is thought that the proteins with a great number of long-range contacts (e.g., β-sheets) follow the L-shaped profile, whereas proteins with predominantly short-range contacts (e.g., helices) follow the diagonal profile.[35] Since chitin fibrils are mainly stabilized by long-range interchain h-bonds, we hypothesized that the self-assembly pathways follow a L-shaped profile.

To test the above hypothesis, we calculated the FES for the formation of individual nanofibril regions listed in Table S1. As order parameters, we used R_g, the number of interchain h-bonds per GlcNAc unit (in analogous to ρ for protein folding), and the percentage solvent exposure (based on solvent accessible surface area or SASA calculations). Interestingly, both L- and diagonal-shaped FES were observed for a single-sheet nanofibril formation. Two examples are given in Figure 4. In the first example, the formation of a 6-chain nanofibril sheet

https://doi.org/10.1021/acs.chemmater.3c01313
Chem. Mater. 2023, 35, 6472−6481

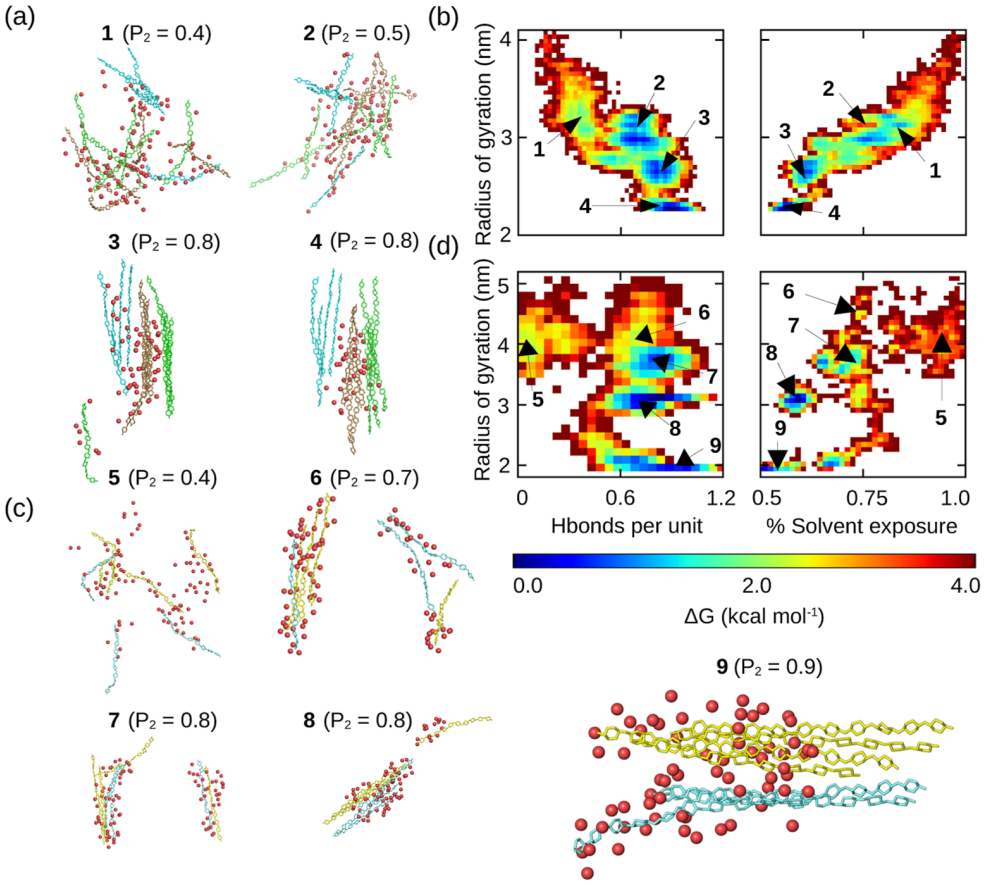

Figure 5. Multisheet nanofibril is assembled by stacking the single-sheet nanofibrils. (a,c) Representative snapshots extracted from the local minimum regions of the FES to illustrate the formation of a 14-chain three-sheet (a, snapshot 1−4) and a 7-chain two-sheet nanofibril (c, snapshot 5−9). Different sheets are indicated by different colors. (b,d) FES spanned by the radius of gyration and the number of interchain h-bonds per GlcNAc unit (left panel) or the percentage solvent exposure (right panel) of the chitin chains. Data for (a,b) and (c,d) refer to the chains in the nanofibril region 3 formed in the 323 K simulation run 2 and 3, respectively.

follows a L-shaped FES, indicating that in the first stage of the self-assembly, the chitin chains move closer together, while the number of interchain h-bonds remains minimal (snapshot 1 and 2 in Figure 4a and FES in Figure 4b left). In this stage, the percentage solvent exposure (which measures the water bound to the chitin chains) of the chitin chains does not significantly change (see FES in Figure 4b right), indicating that while the bulk water is displaced, the chitin chains remain bound to water, that is, the first solvation shell is unperturbed. Consistent with the minimal number of interchain h-bonds, the chains are randomly orientated toward each other (snapshot 1 and 2 in Figure 4a). Following the chain collapse stage, rearrangement of the chains occurs (snapshot 3 and 4 in Figure 4a), which appears to be driven by an increase in the number of interchain h-bonds, while the R_g remains more or less constant (Figure 4b left). At the same time, the percentage solvent exposure of the chains decreases from over 80% to less than 55% (Figure 4b right), indicating that the bound water are expelled as more h-bonds are formed between the chitin chains. With the increase in the number of h-bonds, the chains become more aligned with each other as evident from the increase in the P_2 value. Snapshot 4 shows a 6-chain single-sheet nanofibril (P_2 of 0.9) with most chains perfectly aligned (Figure 4a).

In the second example, the formation of a 10-chain single-sheet nanofibril follows predominantly a diagonal-shaped FES (Figure 4c,d). Although there is an initial descent in the R_g down to the local minimum region 5 (snapshot 5 in Figure 4c) similar to the transition 1 → 2 for the 6-chain fibril, the transition 5 → 6 → 7 → 8 follows a diagonal FES, indicating that as the chains come together the interchain h-bonds form concomitantly (snapshot 5 in Figure 4d, left). This transition is also accompanied by a steep decrease in the percentage solvent exposure, indicating that the first-solvation shell water is expelled from the chains. These data suggest that unlike protein folding, both types of pathways are possible for chitin's nanofibrillation.

To test if there is a change in the chitin chain dimension due to fibrillation, we plotted the probability distribution of the end-to-end distance of the chains in solution (first 50 ns data) and in the nanofibril (final 50 ns data) using the chains that formed a nanofibril sheet at 323 K (data used for Figure 4a,b). The chitin chains in solution (before the self-assembly began) show a broader and slightly left-shifted distribution as compared to the chains in the fibrillar state (Figure 4e). This suggests that the chains are more flexible in solution and they become more extended and rigid (rodlike) when transitioning to the fibrillar state, which is likely a result of the restricted motion due to interchain h-bonding and van der Waals interactions.

The assembly process of multisheet nanofibrils appears to have two stages (two examples are given in Figure 5). In the

https://doi.org/10.1021/acs.chemmater.3c01313
Chem. Mater. 2023, 35, 6472−6481

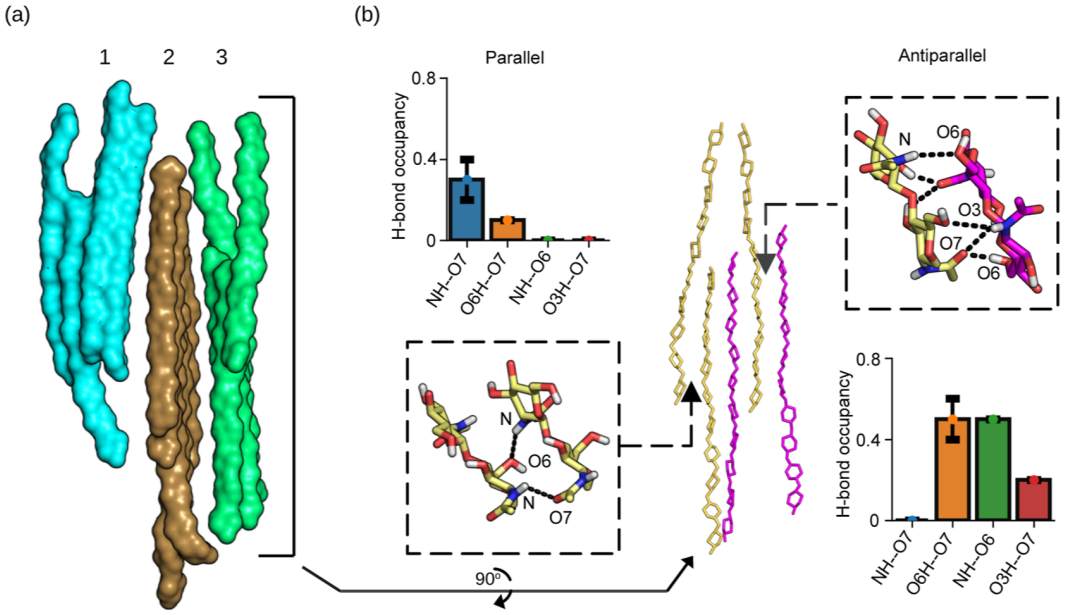

Figure 6. Characterization of the chain orientations and interchain h-bonding in the chitin nanofibril. (a) Snapshot of an example nanofibril (in the van der Waals surface rendering) comprised three sheets, and each sheet has 4−5 chains. Data from the 323 K simulation run 2 is used. (b) Zoomed-in view of sheet 3 (green in a) showing the intrasheet chain orientations and h-bonding. Brown and magenta colors indicate the two chain directions. The occupancies and the zoomed-in views of the specific h-bonds that mediate the parallel and antiparallel chains are given on the left and right panels, respectively. In the zoomed-in view, only two GlcNAc units are shown. The occupancies were calculated from all nanofibril sheets in each of the 323 K runs. The average and standard deviation over the three runs are shown. The final 100 ns of the trajectories was used.

first example, three nanofibril sheets are formed first by following a predominantly diagonal-shaped FES with concomitant chain collapse, interchain h-bond formation, and water expulsion (1 → 2 → 3, Figure 5a,b). In the second stage, the three fibril sheets move closer to form stacking by a small decrease in the solvent exposure (some water in the first solvation shell is expelled), and interestingly, one chain from the solution is added onto one sheet which provides further stabilization (3 → 4, Figure 5a,b). In the second example, two nanofibril sheets are formed first by following a L-shaped FES (5 → 6 → 7, Figure 5c,d). In the second stage, the two sheets move closer to form stacking followed by taking up one chain from solution (7 → 8 → 9, Figure 5c,d). These data suggest that the individual fibril sheets are formed first before intersheet stacking occurs. As a solution chitin chain is added onto a stacked sheet in both examples, we hypothesize that a multisheet nanofibril may serve as a nucleus for chitin's fibril growth similar to amyloid fibrils.[36]

Self-Assembled Nanofibrils are Polymorphic. In nature, chitin can self-assemble into three allomorphs distinguished by the chain alignment, parallel (β), antiparallel (α), and mixed (γ).[10−18] Interestingly, all three allomorphs are observed in the nanofibrils identified in the final "aggregates" (Table S1), which is consistent with the angle analysis showing both parallel and antiparallel chain orientations at 300 and 323 K (Figure 3b). At 300 K, one nanofibril (3 chains) shows parallel, three nanofibrils (3 or 5 chains each) show antiparallel, and two nanofibrils (10 and 13 chains) show mixed alignment. At 323 K, one nanofibril (3 chains) shows parallel, two nanofibrils (3 chains each) show antiparallel, and 6 nanofibrils (3, 14, 21, 10, and 7 chains) show mixed alignment. These data indicate that all three allomorphs are formed. Although the larger nanofibrils formed in the simulations tend to show mixed chain alignment (γ chitin), the preferred orientation is unclear as the simulations were very short and captured only the early self-assembly events.

Specific Interchain Hydrogen Bonds Mediate Fibril Formation and Polymorphism. What forces give rise to the single- and multisheet nanofibrils and the different allomorphs? Interestingly, only the transient O6H...O7 h-bonds were found the nanofibril sheets (Figure S3); instead, the sheet stacking was mainly mediated by van der Waals contacts, suggesting that the hydrophobic effect is dominant for intersheet stabilization (Figure 6a). This is in consistent with the experiments. The X-ray diffraction data of β-chitin demonstrated an absence of h-bonds between the fibril sheets,[16] while a Fourier-transform infrared (FTIR) study suggested that the α-chitin may contain O6′H...O7 h-bonds.[14]

Turning to the intrasheet interactions, we examined specific interchain h-bonds. Surprisingly, despite a large number of interchain h-bonds at 278 K (Figure 3b) , the occupancies of specific h-bonds are very low (the most occupied h-bond O6H...O7 is below 10%, Figure S4), which explains the increased disorder and lack of fibril formation (Figure 3a). By contrast, in the simulations at 300 K and at 323 K, four specific interchain h-bonds, NH...O7, O6H...O7, NH...O6, and O3H...O7, were found and interestingly, parallel and antiparallel chains are stabilized by different h-bonds (Figures 6b and S5). The parallel configurations are stabilized by the NH...O7 h-bond with an occupancy of about 30% (averaged across the three runs at 323 K) and the O6H...O7 h-bond with an occupancy of 10% (Figure 6b, left panel). In contrast, the antiparallel configurations are stabilized by the O6H...O7 (average occupancy ∼50%), NH...O7 (average occupancy ∼50%), and O3H...O7 (average occupancy ∼20%) h-bonds (Figure 6b, right panel). Overall, the antiparallel configurations have more stable interchain h-bonds than the parallel configurations, which provides an explanation for the increased thermal stability[12] and decreased susceptibility to solvent-

https://doi.org/10.1021/acs.chemmater.3c01313
Chem. Mater. 2023, 35, 6472−6481

mediated swelling[19] of α-chitin which is formed by antiparallel chains relative to β-chitin which is formed by parallel chains.

CONCLUSIONS

The MD simulations offered an atomic-level description of how chitin chains self-assemble into nanofibrils from solution at three temperatures. At 278 K, a largely amorphous aggregate without specific interchain h-bonds was formed, whereas at 300 and 373 K, nanofibril regions of various sizes were identified within the final aggregates. At 300 K, single-sheet nanofibrils comprised 3−13 chains were assembled, while at 323 K, nanofibrils with two or three sheets with up to 21 chains in total were assembled. These data are consistent with the recent observation of the heat-induced gelation of chitin dissolved in aqueous KOH/urea.[23,24] The analysis showed that as temperature increases from 278 to 323 K, the total number of intermolecular h-bonds increases and more solvent is expelled from the first-solvation shells of the chitin chains. Further analysis revealed that the single-sheet nanofibril formation of chitin follows either of the two types of pathways: a L-shaped FES profile in which a hydrophobic collapse is followed by maximizing the number of interchain h-bonds while expelling solvent; and the diagonal-shaped FES profile in which the hydrophobic collapse and h-bond formation/solvent expulsion are concomitant. This is surprising, as folding of β-sheet proteins, which are analogous to nanofibrils, is believed to prefer the L-shaped mechanism.[35] Importantly, the multisheet nanofibrils are assembled by stacking the single sheets largely via van der Waals interactions while further excluding solvent.

Considering the correlation between the interchain h-bond formation and water expulsion (release of h-bonded water) and the hydrophobic nature of intersheet stacking, the inverse temperature dependence of chitin's self-assembly may be explained by the hydrophobic effect ($-T\Delta S$) which dominates over the enthalpic contribution (ΔH). This is consistent with a recent study by Durell and Ben-Naim which found that increasing temperature is more favorable for bringing two hydrophilic solutes together that can form direct h-bonds.[34] In the experiments of Cai and co-workers,[23,24] increased temperature may additionally weaken or destroy the interactions of potassium ions and urea with the chitin chains, which further promotes the gelation process. The inverse temperature dependence of chitin's self-assembly is reminiscent of the lower critical solution temperature behavior, for example, elastin-like peptide, which also contains both hydrophobic and hydrophilic residues and undergoes phase transition into peptide-rich and water phase upon heating.[37]

The nanofibrils formed in the simulations captured all three naturally occurring allomorphs of chitin: with all parallel, all antiparallel, or mixed chain orientations. Interestingly, the antiparallel orientation was found to be slightly favored over the parallel orientation. Analysis showed that the different orientations are mediated by different h-bonds with the antiparallel chains forming a larger number of h-bonds, which provides an explanation to the experimental observation that α-chitin (formed only by antiparallel chains) is the most stable allomorph.[13,19] Our data is consistent with the view that the formation of the specific allomorph (α, β, or γ) is due to the microenvironment (e.g., protein wrapping in squid pen) which favors one chain orientation vs the other. One caveat of our study is the use of fully acetylated chitin, whereas in nature chitin may display a low degree of deacetylation. For example, chitin used in the temperature-dependent self-assembly experiment of Cai and co-workers[23,24] was partially deacetylated (less than 20%). However, we do not expect the small difference in the degree of acetylation to affect the qualitative conclusions as the underlying physics remains the same A simulation study of chitin's self-assembly with varying degree and pattern of deacetylation is underway (Romany, Payne, and Shen, unpublished). Taken together, the present study provides a rich, atomic-level view of chitin's self-assembly, which may assist the design of controlled fabrication of chitin-based materials.

METHODS AND PROTOCOLS

All-atom MD simulations were performed using the AMBER20 program.[38] The chitin chains were represented by the CHARMM36 carbohydrate force field.[39,40] Twenty-four chains, each composed of 10 acetylglucosamine units, were randomly distributed using PACKMOL[41] in a 85 Å × 85 Å × 85 Å cubic box filled with the CHARMM-style TIP3P water model.[42] The simulation system comprised approximately 57 978 atoms, and the weight percentage of the chitin was 17.2 wt %, which is about three times the experimental concentration of 6 wt %.[23,24] The higher concentration was used to accelerate the self-assembly and is not expected to affect the mechanisms investigated here. CHAMBER[43] was used to convert the CHARMM parameter and topology files to AMBER format.

A total of 9 simulations were conducted in the system. Three independent simulations were performed for each system at each temperature of the three temperatures (278, 300, or 323 K) starting from different random velocity seeds. The system first underwent energy minimization with a harmonic restraint potential (a force constant of 10 kcal/mol/Å^2) placed on the heavy atom positions. The system was then heated over 1 ns to one of the three temperatures in the *NVT* ensemble. The system was then equilibrated for a total of 100 ns in which the harmonic potential force constant was gradually reduced from 5, 2.5, 1, 0.1 to 0 kcal/mol/Å^2 under constant *NPT* conditions. The temperature was maintained using a Langevin thermostat,[44] and the pressure was maintained at 1 bar using the Monte Carlo barostat.[45] Each production run lasted between 2 and 3 μs under the constant *NPT* conditions. The van der Waals interactions were smoothly switched to zero from 10 to 12 Å. The particle mesh Ewald method[46] was used to calculate long-range electrostatic energies with a sixth-order interpolation and 1 Å grid spacing. Bonds involving hydrogens were constrained using the SHAKE algorithm[47] to enable a 2 fs time steps. Subsequent analysis of simulations was done using cpptraj[48] and VMD.[49]

The relative chain orientation was calculated as

$$\theta = \arccos(\vec{i}\cdot\vec{j}), \tag{1}$$

where $\vec{i}$ is the molecular vector, connecting the center of masses of the second and ninth sugar rings in an individual chain. $\vec{j}$ is the vector of the nearest neighbor chain of $\vec{i}$. If $\theta \approx 0°$, then chains are aligned parallel. If $\theta \approx 180°$, chains are aligned antiparallel. The P_2 order parameter was defined as[31]

$$P_2 = \frac{1}{N}\sum_{i=1}^{N}(\vec{v}_i\cdot\vec{d})^2 \tag{2}$$

$\vec{v}_i$ is the normalized molecular vector connecting the center of mass of the second and ninth sugar rings in an individual chain. $\vec{d}$ is the director, which is a normalized average vector of the unsigned orientations of all individual $\vec{v}_i$. N is the number of molecular vectors (number of chains).

ASSOCIATED CONTENT

Supporting Information

The Supporting Information is available free of charge at https://pubs.acs.org/doi/10.1021/acs.chemmater.3c01313.

https://doi.org/10.1021/acs.chemmater.3c01313
Chem. Mater. 2023, 35, 6472−6481

Detailed information about the nanofibril regions in the simulation runs and additional analysis of the data (PDF)

AUTHOR INFORMATION

Corresponding Author

Jana Shen − *Department of Pharmaceutical Sciences, University of Maryland School of Pharmacy, Baltimore, Maryland 21201, United States;* orcid.org/0000-0002-3234-0769; Email: jana.shen@rx.umaryland.edu

Authors

Aarion Romany − *Department of Pharmaceutical Sciences, University of Maryland School of Pharmacy, Baltimore, Maryland 21201, United States;* orcid.org/0000-0001-5439-8235

Gregory F. Payne − *Institute for Bioscience and Biotechnology Research, University of Maryland, College Park, Maryland 20742, United States;* orcid.org/0000-0001-6638-9459

Complete contact information is available at: https://pubs.acs.org/10.1021/acs.chemmater.3c01313

Notes

The authors declare no competing financial interest.

ACKNOWLEDGMENTS

Financial support from the National Science Foundation (CBET1932963) is acknowledged.

REFERENCES

(1) Goycoolea, F. M.; Argüelles-Monal, W.; Peniche, C.; Higuera-Ciapara, I. Chitin and Chitosan. *Develop. Food Sci* **2000**, *41*, 265−308.

(2) Barber, P. S.; Shamshina, J. L.; Rogers, R. D. A "Green"' Industrial Revolution: Using Chitin towards Transformative Technologies. *Pure Appl. Chem.* **2013**, *85*, 1693−1701.

(3) Elieh-Ali-Komi, D.; Hamblin, M. R. Chitin and Chitosan: Production and Application of Versatile Biomedical Nanomaterials. *Int. J. Adv. Res.* **2016**, *4*, 411−427.

(4) Lee, S.; Hao, L. T.; Park, J.; Oh, D. X.; Hwang, D. S. Nanochitin and Nanochitosan: Chitin Nanostructure Engineering with Multiscale Properties for Biomedical and Environmental Applications. *Adv. Mater.* **2023**, *35*, 2203325.

(5) Bai, L.; Huan, S.; Xiang, W.; Liu, L.; Yang, Y.; Nugroho, R. W. N.; Fan, Y.; Rojas, O. J. Self-Assembled Networks of Short and Long Chitin Nanoparticles for Oil/Water Interfacial Superstabilization. *ACS Sustain. Chem. Eng.* **2019**, *7*, 6497−6511.

(6) Cord-Landwehr, S.; Moerschbacher, B. M. Deciphering the ChitoCode: Fungal Chitins and Chitosans as Functional Biopolymers. *Fungal Biol. Biotechnol.* **2021**, *8*, 19.

(7) Maddaloni, M.; Vassalini, I.; Alessandri, I. Green Routes for the Development of Chitin/Chitosan Sustainable Hydrogels. *Sustain. Chem.* **2020**, *1*, 325−344.

(8) Kadokawa, J.-i. Preparation of Composite Materials from Self-Assembled Chitin Nanofibers. *Polymers* **2021**, *13*, 3548.

(9) Narkevicius, A.; Steiner, L. M.; Parker, R. M.; Ogawa, Y.; Frka-Petesic, B.; Vignolini, S. Controlling the Self-Assembly Behavior of Aqueous Chitin Nanocrystal Suspensions. *Biomacromolecules* **2019**, *20*, 2830−2838.

(10) Blackwell, J. Structure of β-Chitin or Parallel Chain Systems of Poly-?-(1?4)-N-acetyl-D-glucosamine. *Biopolymers* **1969**, *7*, 281−298.

(11) Neville, A.; Parry, D.; Woodhead-Galloway, J. The Chitin Crystallite in Arthropod Cuticle. *J. Cell Sci.* **1976**, *21*, 73−82.

(12) Sugiyama, J.; Boisset, C.; Hashimoto, M.; Watanabe, T. Molecular Directionality of β-Chitin Biosynthesis. *J. Mol. Biol.* **1999**, *286*, 247−255.

(13) Jang, M.-K.; Kong, B.-G.; Jeong, Y.-I.; Lee, C. H.; Nah, J.-W. Physicochemical Characterization of α-Chitin, β-Chitin, and γ-Chitin Separated from Natural Resources. *J. Polym. Sci., A: Polym. Chem.* **2004**, *42*, 3423−3432.

(14) Sikorski, P.; Hori, R.; Wada, M. Revisit of Alpha-Chitin Crystal Structure Using High Resolution X-Ray Diffraction Data. *Biomacromolecules* **2009**, *10*, 1100−1105.

(15) Nishiyama, Y. Structure and Properties of the Cellulose Microfibril. *J. Wood Sci.* **2009**, *55*, 241−249.

(16) Nishiyama, Y.; Noishiki, Y.; Wada, M. X-Ray Structure of Anhydrous β-Chitin at 1 Å Resolution. *Macromolecules* **2011**, *44*, 950−957.

(17) Sawada, D.; Nishiyama, Y.; Langan, P.; Forsyth, V. T.; Kimura, S.; Wada, M. Water in Crystalline Fibers of Dihydrate β-Chitin Results in Unexpected Absence of Intramolecular Hydrogen Bonding. *PLoS One* **2012**, *7*, No. e39376.

(18) Kaya, M.; Mujtaba, M.; Ehrlich, H.; Salaberria, A. M.; Baran, T.; Amemiya, C. T.; Galli, R.; Akyuz, L.; Sargin, I.; Labidi, J. On Chemistry of γ-Chitin. *Carbohydr. Polym.* **2017**, *176*, 177−186.

(19) Rinaudo, M. Chitin and chitosan: Properties and applications. *Prog. Polym. Sci.* **2006**, *31*, 603−632.

(20) Fan, Y.; Saito, T.; Isogai, A. Preparation of Chitin Nanofibers from Squid Pen β-Chitin by Simple Mechanical Treatment under Acid Conditions. *Biomacromolecules* **2008**, *9*, 1919−1923.

(21) Ehren, H. L.; Appels, F. V. W.; Houben, K.; Renault, M. A. M.; Wösten, H. A. B.; Baldus, M. Characterization of the Cell Wall of a Mushroom Forming Fungus at Atomic Resolution Using Solid-State NMR Spectroscopy. *Cell Surf.* **2020**, *6*, 100046.

(22) Fernando, L. D.; Dickwella Widanage, M. C.; Penfield, J.; Lipton, A. S.; Washton, N.; Latgé, J.-P.; Wang, P.; Zhang, L.; Wang, T. Structural Polymorphism of Chitin and Chitosan in Fungal Cell Walls From Solid-State NMR and Principal Component Analysis. *Front. Mol. Biosci.* **2021**, *8*, 727053.

(23) Huang, J.; Zhong, Y.; Lu, A.; Zhang, L.; Cai, J. Temperature and Time-Dependent Self-Assembly and Gelation Behavior of Chitin in Aqueous KOH/Urea Solution. *Giant* **2020**, *4*, 100038.

(24) Huang, J.; Zhong, Y.; Wei, P.; Cai, J. Rapid Dissolution of β-Chitin and Hierarchical Self-Assembly of Chitin Chains in Aqueous KOH/Urea Solution. *Green Chem.* **2021**, *23*, 3048−3060.

(25) Beckham, G. T.; Crowley, M. F. Examination of the α-Chitin Structure and Decrystallization Thermodynamics at the Nanoscale. *J. Phys. Chem. B* **2011**, *115*, 4516−4522.

(26) Strelcova, Z.; Kulhanek, P.; Friak, M.; Fabritius, H.-O.; Petrov, M.; Neugebauer, J.; Koca, J. The Structure and Dynamics of Chitin Nanofibrils in an Aqueous Environment Revealed by Molecular Dynamics Simulations. *RSC Adv.* **2016**, *6*, 30710−30721.

(27) Hudek, M.; Kubiak-Ossowska, K.; Johnston, K.; Ferro, V. A.; Mulheran, P. A. Chitin and Chitosan Binding to the α-Chitin Crystal: A Molecular Dynamics Study. *ACS Omega* **2023**, *8*, 3470−3477.

(28) Wei, A.; Fu, J.; Guo, F. Mechanical Properties of Chitin Polymorphs: A Computational Study. *J. Mater. Sci.* **2021**, *56*, 12048−12058.

(29) Tsai, C.-C.; Morrow, B. H.; Chen, W.; Payne, G. F.; Shen, J. Toward Understanding the Environmental Control of Hydrogel Film Properties: How Salt Modulates the Flexibility of Chitosan Chains. *Macromolecules* **2017**, *50*, 5946−5952.

(30) Zhang, W.; Turney, T.; Meredith, R.; Pan, Q.; Sernau, L.; Wang, X.; Hu, X.; Woods, R. J.; Carmichael, I.; Serianni, A. S. Conformational Populations of β-(1 → 4) O-Glycosidic Linkages Using Redundant NMR J-Couplings and Circular Statistics. *J. Phys. Chem. B* **2017**, *121*, 3042−3058.

(31) Wallace, J. A.; Shen, J. K. Probing the Strand Orientation and Registry Alignment in the Propagation of Amyloid Fibrils. *Biochemistry* **2010**, *49*, 5290−5298.

(32) Schellman, J. A. Temperature, Stability, and the Hydrophobic Interaction. *Biophys. J.* **1997**, *73*, 2960−2964.

(33) Southall, N. T.; Dill, K. A.; Haymet, A. D. J. A View of the Hydrophobic Effect. *J. Phys. Chem. B* **2002**, *106*, 521−533.

(34) Durell, S. R.; Ben-Naim, A. Temperature Dependence of Hydrophobic and Hydrophilic Forces and Interactions. *J. Phys. Chem. B* **2021**, *125*, 13137−13146.
(35) Shea, J.-E.; Brooks III, C. L. FROM FOLDING THEORIES TO FOLDING PROTEINS: A Review and Assessment of Simulation Studies of Protein Folding and Unfolding. *Annu. Rev. Phys. Chem.* **2001**, *52*, 499−535.
(36) Buell, A. K.; Dhulesia, A.; White, D. A.; Knowles, T. P. J.; Dobson, C. M.; Welland, M. E. Detailed Analysis of the Energy Barriers for Amyloid Fibril Growth. *Angew. Chem., Int. Ed.* **2012**, *51*, 5247−5251.
(37) Li, N. K.; Quiroz, F. G.; Hall, C. K.; Chilkoti, A.; Yingling, Y. G. Molecular Description of the LCST Behavior of an Elastin-Like Polypeptide. *Biomacromolecules* **2014**, *15*, 3522−3530.
(38) Case, D. A.; Ben-Shalom, I. Y.; Brozell, S. R.; Cerutti, D. S.; Cheatham, T., III; Cruzeiro, V. W. D.; Darden, T. A.; Duke, R. E.; Ghoreishi, D.; Gilson, M. K.; Gohlke, H.; Goetz, A. W.; Greene, D.; Harris, R.; Homeyer, N.; Huang, Y.; Izadi, S.; Kovalenko, A.; Kurtzman, T.; Lee, T. S.; LeGrand, S.; Li, P.; Lin, C.; Liu, J.; Luchko, T.; Luo, R.; Mermelstein, D. J.; Merz, K. M.; Miao, Y.; Monard, G.; Nguyen, C.; Nguyen, H.; Omelyan, I.; Onufriev, A.; Pan, F.; Qi, R.; Roe, D. R.; Roitberg, A.; Sagui, C.; Schott-Verdugo, S.; Shen, J.; Simmerling, C. L.; Smith, J.; Salomon-Ferrer, R.; Swails, J.; Walker, R. C.; Wang, J.; Wei, H.; Wolf, R. M.; Wu, X.; Xiao, L.; York, D. M.; Kollman, P. A. *AMBER 2020*; University of California: San Francisco, 2020;.
(39) Guvench, O.; Greene, S. N.; Kamath, G.; Brady, J. W.; Venable, R. M.; Pastor, R. W.; Mackerell, A. D. Additive Empirical Force Field for Hexopyranose Monosaccharides. *J. Comput. Chem.* **2008**, *29*, 2543−2564.
(40) Guvench, O.; Mallajosyula, S. S.; Raman, E. P.; Hatcher, E.; Vanommeslaeghe, K.; Foster, T. J.; Jamison, F. W.; MacKerell, A. D. CHARMM Additive All-Atom Force Field for Carbohydrate Derivatives and Its Utility in Polysaccharide and Carbohydrate−Protein Modeling. *J. Chem. Theory Comput.* **2011**, *7*, 3162−3180.
(41) Martinez, L.; Andrade, R.; Birgin, E.; Martinez, J. Packmol: A Package for Building Initial Configurations for Molecular Dynamics Simulations. *J.Comput.Chem* **2009**, *30*, 2157−2164.
(42) Brooks, B.; Brooks, C.; MacKerell, A.; Nilsson, L.; Petrella, R.; Roux, B.; Won, Y.; Archontis, G.; Bartels, C.; Boresch, S.; Caflisch, A.; Caves, L.; Cui, Q.; Dinner, A.; Feig, M.; Fischer, S.; Gao, J.; Hodoscek, M.; Im, W.; Kuczera, K.; Lazaridis, T.; Ma, J.; Ovchinnikov, V.; Paci, E.; Pastor, R.; Post, C.; Pu, J.; Schaefer, M.; Tidor, B.; Venable, R. M.; Woodcock, H. L.; Wu, X.; Yang, W.; York, D.; Karplus, M. CHARMM: The Biomolecular Simulation Program. *J. Comput. Chem.* **2009**, *30*, 1545−1614.
(43) Shirts, M. R.; Klein, C.; Swails, J. M.; Yin, J.; Gilson, M. K.; Mobley, D. L.; Case, D. A.; Zhong, E. D. Lessons Learned from Comparing Molecular Dynamics Engines on the SAMPL5 Dataset. *J.Comput.-Aided Mol.Des.* **2017**, *31*, 147−161.
(44) Grønbech-Jensen, N.; Farago, O. A Simple and Effective Verlet-type Algorithm for Simulating Langevin Dynamics. *Mol. Phys.* **2013**, *111*, 983−991.
(45) Chow, K.-H.; Ferguson, D. M. Isothermal-Isobaric Molecular Dynamics Simulations with Monte Carlo Volume Sampling. *Comput. Phys. Commun.* **1995**, *91*, 283−289.
(46) Darden, T.; York, D.; Pedersen, L. Particle Mesh Ewald: An $N \cdot \log(N)$ Method for Ewald Sums in Large Systems. *J. Chem. Phys.* **1993**, *98*, 10089−10092.
(47) Miyamoto, S.; Kollman, P. A. Settle: An Analytical Version of the SHAKE and RATTLE Algorithm for Rigid Water Models. *J. Comput. Chem.* **1992**, *13*, 952−962.
(48) Roe, D. R.; Cheatham, T. E. PTRAJ and CPPTRAJ: Software for Processing and Analysis of Molecular Dynamics Trajectory Data. *J. Chem. Theory Comput.* **2013**, *9*, 3084−3095.
(49) Humphrey, W.; Dalke, A.; Schulten, K. VMD: Visual Molecular Dynamics. *J. Mol. Graphics* **1996**, *14*, 33−38.

https://doi.org/10.1021/acs.chemmater.3c01313
Chem. Mater. 2023, 35, 6472−6481